FULL RESEARCH ARTICLE

Controlling the mechanical properties of laser powder bed fusion manufactured AlSi10Mg using optimized oscillating scan paths

Samuel Meyer[1] · Lukas Englert[1] · Philipp Schüßler[1] · Volker Schulze[1] · Stefan Dietrich[1]

Abstract

In the field of metal additive manufacturing, laser powder bed fusion (L-PBF) stands out for its maturity. The path the laser takes over the powder, in this study AlSi10Mg, is determined by a large set of separate parameters; the combination of which offers ample room for optimization. The close ties between the parameters chosen, and the resulting mechanical properties, are what motivates the extensive research done in this field. This study changed the scan line path into a circular oscillation (prolate trochoid) and narrows down a large set of parameters to two sets that exhibit significant differences from traditional scan lines in terms of density, porosity distribution, tensile strength, elongation at fracture, hardness, surface roughness, and melt pool (MP) shape. Remarkable upper bounds for MP size were also characterized for the first time in this work. Some of the noteworthy findings consist of an up to 70% reduction in surface roughness, up to a 40% increase in the elongation at fracture, and up to a 150 µm range of hatching distances to produce a part with under 0.5% porosity. The last of which leads to an overall increase in the robustness of the L-PBF manufacturing process by reducing the sensitivity to parameter fluctuations.

Keywords Selective laser melting (SLM) · Laser beam powder bed fusion (PBF-LB) · Mechanical properties · AlSi10Mg · Spatial power modulation

1 Introduction

Since the shift from viewing laser powder bed fusion (L-PBF) as a budding technology to an established way of manufacturing final products, the need for research that addresses the optimization of said technology has gained importance. In L-PBF a metal powder is spread across a printing bed, and a laser iteratively melts a single layer into a consolidated object. Layer-by-layer complex geometries are fused together without the investment into a casting mold allowing for intricate designs, reduction in material use through the collection of unused powder, and a fine, high-strength microstructure resulting from rapid cooling rates. While the manufacturing process is already used for small series production, the melt pool (MP) that forms around the laser's entry point into the powder bed is a volatile and sensitive environment that is not fully understood, yet. Optimizing laser parameters that produce consistently dense, crack-less, and smooth parts is a focus in the field of research [1]. Whether it is the foundational experimentation done by Buchbinder et al., Yadroitsev and Smurov [2, 3], the cutting-edge high-fidelity modeling used by Bayat et al. [4], or the deep neural networks developed by Xing et al. [5] the goal is to identify a process window. More than ten different parameters have to be balanced to achieve fusion of the new layer with the previous layers, while avoiding keyhole instabilities [4, 6]. Only a small parameter window, which can even be shifted mid-print due to optical components, has been found to create desirable properties [7, 8].

Since L-PBF is essentially a laser welding process, recent L-PBF research has borrowed scan strategies from the more

✉ Lukas Englert
  lukas.englert@kit.edu

  Samuel Meyer
  samuel.meyer@student.kit.edu

  Philipp Schüßler
  philipp.schuessler@kit.edu

  Volker Schulze
  volker.schulze@kit.edu

  Stefan Dietrich
  stefan.dietrich@kit.edu

[1] Institute for Applied Materials-Materials Science and Engineering (IAM-WK), Karlsruhe Institute of Technology, Engelbert-Arnold-Straße 4, 76131 Karlsruhe, Germany

🍂 Springer

mature laser welding technology. For example, the laser in a laser welding machine can follow a non-linear path over the workpiece [9, 10]. Circular laser oscillation has proven to be a promising scan strategy for producing welds with the desired mechanical properties [11]. Due to the slower cooling rates in the larger MPs, circular oscillations in the field of laser welding with the aluminum alloy AA6061-T6 have been found to increase the elongation at fracture by 38% [12]. Börner et al. found through an in situ x-ray analysis that high-frequency beam oscillation encouraged keyhole degassing, which reduced porosity in aluminum laser welds [13]. Lastly, due to the larger width of the weld MPs using beam oscillation, Choi et al. discovered an increased shear-tensile strength due to the increased amount of fused metal between the weld members [14].

The periodic path followed by the laser commonly used when referring to circular oscillation is called a trochoid; the pattern comes from the line created when one point of a circle is traced as it is rolling. More specifically, this shape is considered a prolate trochoid because the point being traced lies outside the rolling circle. The motivation behind the use of an oscillating laser pattern in L-PBF is to remelt recently solidified parts of the laser path to give pores the ability to escape and to change the overall mechanical properties due to a larger MP [12]. Moreover, the additional dimension of the laser movement increases the turbulence of the MP, which promotes the release of micropores filled with metal vapor [15]. Both theories point towards advantageous properties. Furthermore, fluid flow in the MP is theorized to help break apart the aluminum oxide layers on both the molten metal and solid metal to increase wettability [16]. Furthermore, the additional width of the MP could stabilize the molten material to reduce the chance of balling due to the larger ratio of MP width to length. This decreases the likelihood of Plateau-Rayleigh instability by increasing the circumference of the liquid cylinder [17, 18]. Lastly, using an oscillating scan path has been found to reduce the surface roughness of stainless steel and Permalloy parts [19, 20].

The increased thermal conductivity and lower absorption coefficient of aluminum compared to other commonly used AM metals exacerbates the aforementioned difficulty of finding a fitting parameter set [21]. Additionally, the aluminum-oxide layer that aluminum alloys form on their surface decreases laser absorptivity and increases the chance of balling [16]. On the other hand, aluminum has a novel microstructure when fabricated with an L-PBF process due to cooling rates on the order of $10^6 \, \text{K s}^{-1}$ [22, 23]. The resulting ultrafine cell structure increases the hardness and tensile strength compared to traditionally cast parts [24, 25]. This cell structure has also been found to be affected by the laser parameters selected for manufacturing [26, 27]. This study presents the hypothesis that the advantageous findings of using oscillating scanning lines and the malleable cell structure of AlSi10Mg using targeted scanning parameters can be combined to actively steer mechanical properties.

This study provides a comprehensive analysis of circular oscillation parameters and their effect on the mechanical properties of AlSi10Mg samples. This has never been researched in the existing literature and fills a vital gap for this common Al alloy. Through the use of single MPs, cubes, and tensile strength specimens, a full factorial set of parameters was narrowed down to two sets that exhibit significant differences from traditional scan lines in terms of density, porosity distribution, tensile strength, elongation at fracture, hardness, surface roughness, and MP shape. The result of this study will lay out a stable range of parameters, as well as describe the effects that using this novel scan strategy has on the AlSi10Mg final product's mechanical properties.
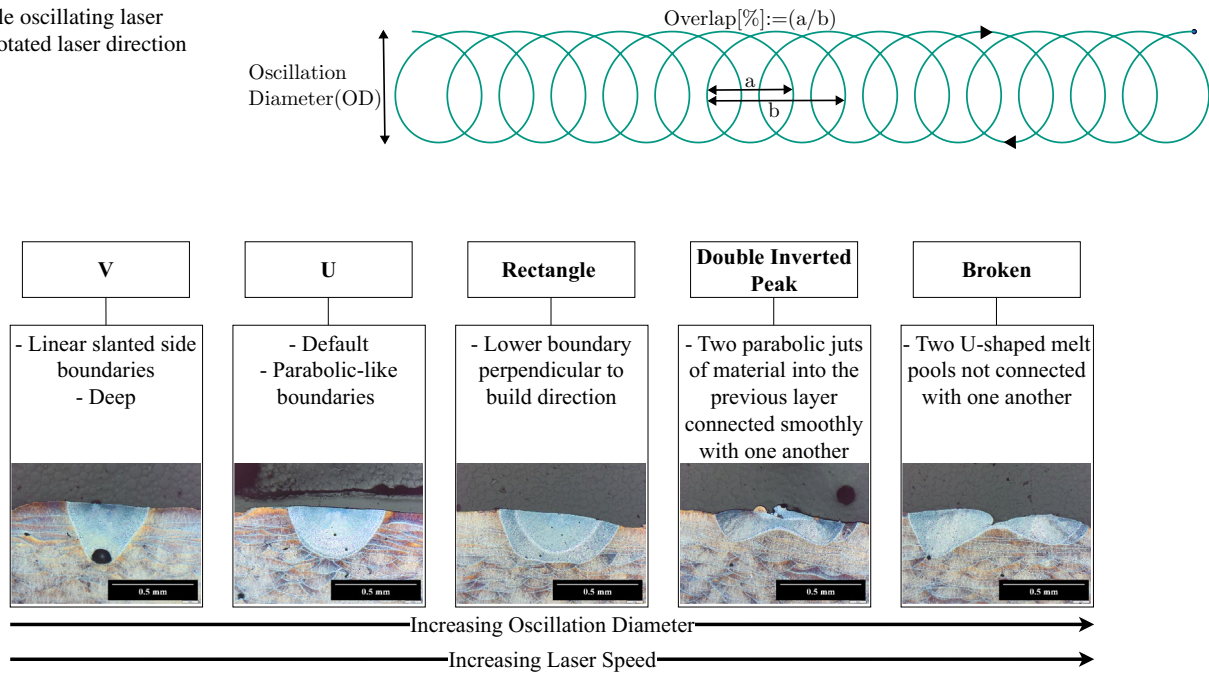
2 Methods

2.1 Experimental design

To optimize the parameters associated with circular laser oscillations, multiple separate specimens were used. Single MPs were printed on a previously additively manufactured 2 mm thick plate, to achieve a realistic powder layer thickness for the process. This was done to rule out mismatched parameters using a mostly qualitative selection process. This process is similar to the one used by Yang et al. to optimize the circular oscillation frequency with Inconel 718 samples using a custom L-PBF machine or the single-track analysis performed by Yadroitsev and Smurov [3, 15]. The same AlSi10Mg powder was used for all samples manufactured in this study: a gas atomized powder supplied by m4p Material Solutions GmbH with D10, D50, and D90 values of 21.0 μm, 35.3 μm, and 57.5 μm respectively. The chemical composition is described in Table 1.

The ORLAS Creator from O.R. Laser Technologie GmbH, equipped with a 250-Watt Yb fiber laser, was used to manufacture all samples present in this study. Argon was used as an inert shielding gas. The accompanying software, ORLAS Suite version 6.1.0.13, was used to process and slice the.stl files of the sample geometry. A 67° layer rotation, 30 μm layer thickness, and 250 W

Table 1 Chemical composition of the given AlSi10Mg powder in wt.%

Al	Si	Mg	Fe	Ti	Zn	Mn	Cu	Pb	Sn	Ni
Base	9.8	0.31	0.14	0.01	0.01	< 0.01	< 0.01	< 0.01	< 0.01	< 0.01

Fig. 1 Single oscillating laser path with notated laser direction

Overlap[%]:=(a/b)

Oscillation Diameter(OD)

V	U	Rectangle	Double Inverted Peak	Broken
- Linear slanted side boundaries - Deep	- Default - Parabolic-like boundaries	- Lower boundary perpendicular to build direction	- Two parabolic juts of material into the previous layer connected smoothly with one another	- Two U-shaped melt pools not connected with one another

Increasing Oscillation Diameter

Increasing Laser Speed

Fig. 2 Characteristics of melt pool shapes and influential parameters

laser power were all kept constant throughout this study. Each cube was fabricated using a single contour scan line, consistent with the hatching parameters.

2.1.1 Single MPs

Single MPs were used to contain a large number of parameters from a full-factorial parameter decomposition. The absolute laser speed along the scan path, the oscillation diameter (OD), and the overlap of the oscillating laser path were varied. $1000 \, \text{mm} \, \text{s}^{-1}$ and $2000 \, \text{mm} \, \text{s}^{-1}$ were used alongside an OD range from 100 to 900 µm in 100 µm steps as well as an overlap range from 20 to 80% in 20% steps. Oscillation overlap is the term that describes the amount the new loop overlaps the last loop in percent as seen in Fig. 1. Additionally, to describe the MP shape this study coins the terms "V", "U", and broken MP shapes in addition to the already in-use shapes: rectangle and inverted peaks used by Yang et al. [15]. The properties of each shape that define the classification are shown in Fig. 2 as well as the two process parameters that influence them. The width, depth, and height were measured using the ImageJ [28] software suite. Furthermore, the MPs were then outlined manually, and the area was measured. Lastly, some MPs showed obvious signs of keyhole instability with the presence of relatively large pores; these parameter sets were ruled out.

Table 2 Three parameter sets chosen to manufacture cubes with variable hatch distances

Abbr	OD in µm	Overlap in %	Speed in mm/s
C60	400	60	1000
C80	500	80	2000
C40	300	40	2000

2.1.2 Cuboid samples

From the narrowed-down set of single MPs outlined in Table 2, $1 \times 1 \times 1 \, \text{cm}^3$ cubes with a single contour scan were fabricated while varying the hatching distance between individual oscillating laser paths. The starting hatching distance was the width of the single MP rounded down to the next 10 µm step because typical scan patterns are printed with a hatching overlap between scan lines. Subsequent cubes increased and decreased the hatching distance in 30 µm steps. Two separate sets of 24 cubes were needed to span the given parameters while also manufacturing every cube twice to reduce error. For each build plate, two control cubes were also printed with parameters that are known from previous studies to create high-density parts with this study's L-PBF machine and AlSi10Mg powder [29].

These cubes were used to further narrow the parameter pool for optimal performance based on surface roughness, density using the Archimedes method, porosity analysis

using micro-computed tomography (μCT) scans, HV1 microhardness, and microstructure analysis with a polished and etched cross-section.

2.1.3 Tensile strength specimens

Standardized specimen in accordance with ISO 6892-1 in form D with a test length of 33 mm and a diameter of 4 mm based on ISO 50125 were used to measure strength and ductility [30]. The C80 parameter set with a hatching distance of 450 μm was selected because it possessed the lowest surface roughness values. The C40 parameter set with a hatching distance of 240 μm was selected because it possessed the highest HV1 hardness values. Ten specimens without oscillating scan lines as a control and ten specimens of each of the two chosen parameter sets were tested. To minimize the error resulting from build plate positioning, the parameters were rotated. These specimens were used to determine the ultimate tensile strength, the yield strength, and the elongation at fracture (see Table 3).

2.2 Analysis

2.2.1 Surface roughness

The μsurf confocal microscope from Nanofocus was used to measure the surface roughness over an 18 mm^2 area automatically in accordance with ISO 25178 [31]. This was done by stitching a 3×3 arrangement of 2 mm^2 measurements together to reduce the effect of outliers, such as spatter particles, on the results. 24 cubes were tested from the middle of the hatch distance range. The accompanying μsoft software was used to interpret, crop, level, and visually represent the data.

2.2.2 Porosity

μCT scans were made using the YXLON Precision μCT equipped with the Perkin Elmer XRD1620 AN flat panel detector with a resolution of 2048×2048 pixels. Four separate specimens were selected for the scans: the cube with the best surface roughness values, the cube with one of the highest microhardness HV1 values, one control cube, and

one tensile strength specimen that possessed the largest MPs of the set. The cubes were scanned with a voxel edge length of 8.7 μm and an acceleration voltage of 165 kV and a current of 0.06 mA. The analysis of these scans was done exclusively with VGstudio Max version 3.4.2 developed by Volume Graphics GmbH. More specifically, the pore analysis was performed with the EasyPore algorithm.

The relative density values used in this study were attained using the Archimedes density method. All weights, in air and submerged in water, were measured to an accuracy of 0.1 mg. To avoid bubbles trapped on the surface of the samples that skew density values, every sample was rotated and gently moved while submerged to allow the bubbles to detach. The density values were then established relative to the AlSi10Mg density given by the powder supplier used in this study: 2.67 g/cm^3.

2.2.3 Mechanical properties

The aforementioned ultimate tensile strength, yield strength, and the elongation at the point of fracture values were collected using the ZwickRoell ZMART.PRO equipped with an Xforce P 20 kN load cell. For accurate elongation values, a MultiXtens extensometer was attached to the samples. The test was carried out while following the procedure outlined in ISO 6892-1 using a constant traverse speed described by the A2 procedure [30]. Data analysis was performed with the help of the accompanying TestXpert II software. The diameter measurements needed for accurate stress measurements were acquired using an optical measurement taken from a microscope image for each specimen. This reduces the error associated with a manual measurement due to the rough surface of parts created using AM.

Vickers Hardness values in this study were attained using a Qness Q30a+, ATM Qness GmbH equipped with a Vickers diamond indenter. An automatic testing series of 10 data points, arranged on a 5x2 grid, was collected and analyzed using the accompanying Qpix software. This was done for all 12 cubes, including two control cubes, which received a polished cross-section.

2.2.4 Microstructure

Samples were polished down to a 1 μm diamond suspension and a subsequent active oxide polishing suspension. A 2% NaOH solution was used to etch the samples for 90 s. Scanning electron microscopy was carried out using a Leo 50 (Carl Zeiss AG) with an acceleration voltage of 10 kV and a secondary electron detector to capture images of the

Table 3 The three parameter sets chosen to manufacture tensile strength specimens

Abbr	OD in μm	Overlap in %	Speed in mm s^{-1}	Hatch Distance in μm
C40	300	40	2000	240
C80	500	80	2000	450
Control			1000	130

etched cross-sections. Average grain size was measured in accordance with ASTM E 112-96 [32].

3 Results

3.1 MP shape

At a significant OD, the peaks and troughs of the oscillation have already solidified by the time the laser returns to that area. The pictures used to place the transition point

at a hatching distance of 600 µm for the 1000 mm s^{-1}, 40% overlap parameter series is pictured in Fig. 3. The gaps between oscillation loops, pointing towards a disjoint MP, are seen in the last three MPs of Fig. 3. 62 of the 72 single MPs observed had a unified MP.

As the OD increased, the width of the MP also increased, as shown in Fig. 4. For a general reference to the width difference to a traditional scan line, the control scan line width used for the rest of this study is 209 µm. The disjoint MPs in Fig. 4 are plotted as a cross instead of a circle. All
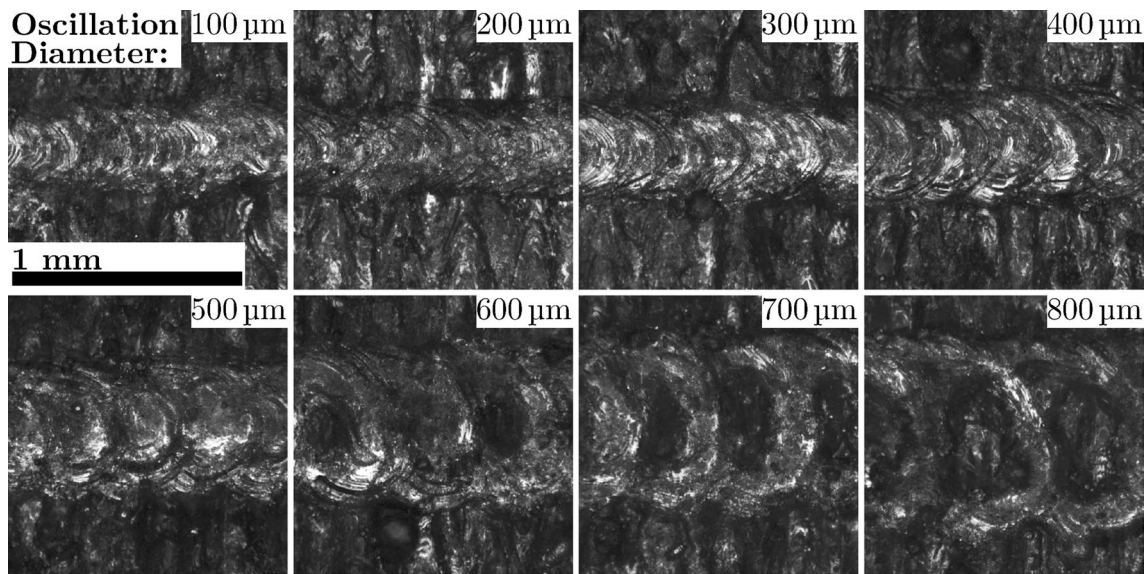
Fig. 3 40% overlap, 1000 mm s^{-1} scan speed with variable OD

(a)

(b)
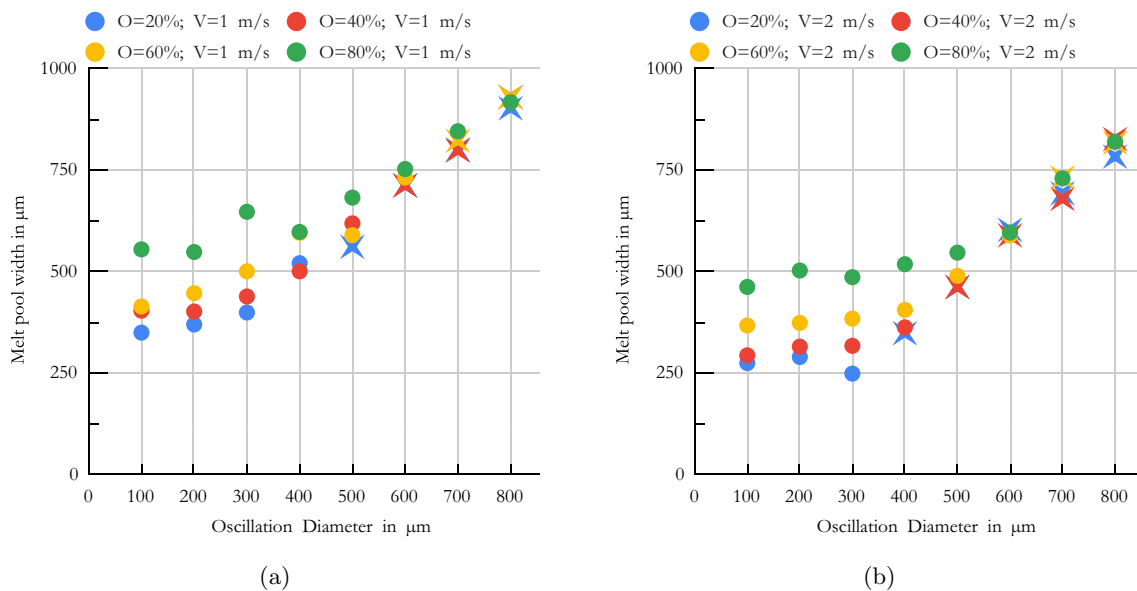
Fig. 4 Melt pool width with varied OD (a): 1000 mm s^{-1} scan speed, (b): 2000 mm s^{-1} scan speed. Disjoint melt pools are plotted with a cross

parameter sets exhibit this transition point unless the overlap is high enough to not allow the possibility of a gap between oscillations. For example, at a scan speed of 1000 mm s^{-1}, the series of parameters with overlaps of 20% and 60% had a transition point of 500 µm and 700 µm respectively. Even at a scan speed of 2000 mm s^{-1}, 80% overlap did not have a transition point in the diameter range observed. The laser scan speed also has a noticeable effect on the MP width. The comparison between Fig. 4a and Fig. 4b shows that when the laser spends less time depositing energy into the powder and previous layers, the MP shrinks.

Another correlation observed by the single MPs manufactured in this study is between MP depth and OD, as seen in Fig. 5. Because the parameter sets with disjoint MPs were already ruled out before the cross-section was ground and polished to measure the MP depth, not all eight data points are present for the four parameter sets pictured. Like an increase in the MP width, an increase in the scan speed decreases the depth of the MP. The less time the laser has to deposit its energy onto the metal, the less it penetrates through the material. This is seen in the comparison between Fig. 5a and Fig. 5b.

The average depth of the MPs that were excluded from further investigation due to obvious signs of porosity had an average MP depth of 0.41 mm, while the parameter sets that were not excluded had an average depth of 0.24 mm as seen in Fig. 6.

Polished and etched cross-sections were used to analyze the shape of the resulting MPs. As seen in Fig. 2 five different shapes were used for the classification: V, U, rectangular, inverted double peak, and broken shapes. Opposed to a normal linear scan line which always has a predictable
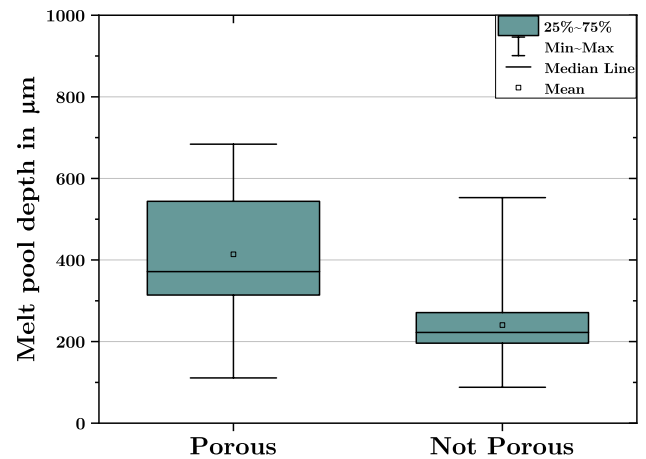

Fig. 6 Depth distribution of all melt pools created using circular oscillating scan lines

U-shape, circular oscillations open the door to other shapes. Furthermore, MPs with rectangular MP shapes did not show obvious keyhole instability. All parameter sets followed the same MP shape progression as seen in Fig. 2. In other words, a double inverted peak never appeared before a U-shape when stepping up the OD. This can be seen in Table 4 with all disjoint MPs removed.

Between the above-described keyhole instability and the disjoint MP, an optimal zone exists, which narrows down the parameter sets. Of the 72 single MPs tested only 14 made it through the selection process and of those, a diverse selection was made to gather the most possible information about circular oscillation scan lines using aluminum L-PBF manufacturing: C60 [60% overlap,
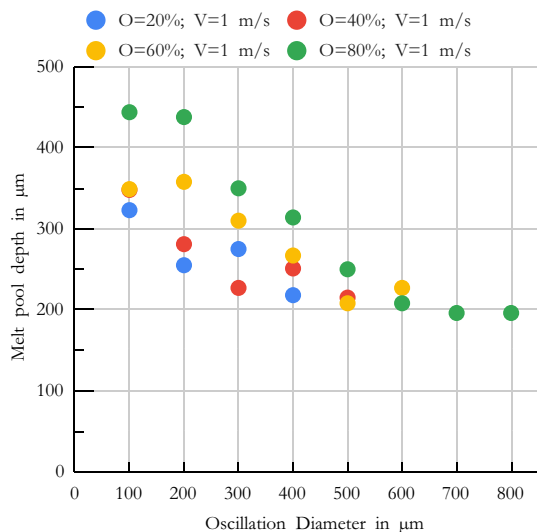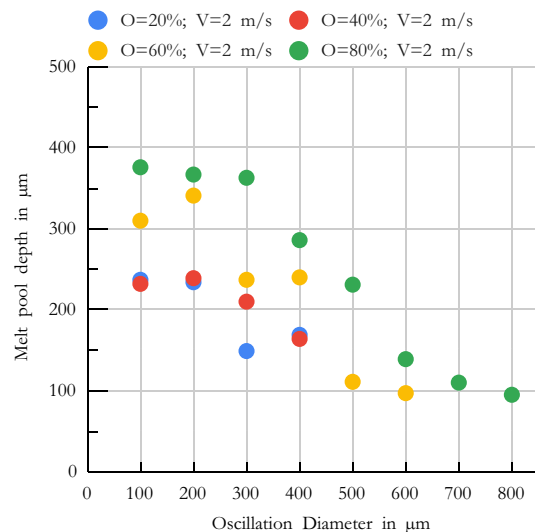

Fig. 5 Melt pool depth with varied OD **a** 1000 mm s^{-1} scan speed, **b** 2000 mm s^{-1} scan speed

Table 4 Melt pool shape with the change in OD: v = V-shape; u = U-shape; r = rectangular shape; d = double inverted peak; b = broken melt pool

Parameter set	OD in µm							
	100	200	300	400	500	600	700	800
O = 20%; V = 1 m s^{-1}	v	u	u	r	r			
O = 20%; V=2 m s^{-1}	v	v	u	u				
O = 40%; V = 1 m s^{-1}	v	u	u	r	r			
O = 40%; V = 2 m s^{-1}	v	v	u	u				
O = 60%; V = 1 m s^{-1}	v	u	u	r	r	r	d	
O = 60%; V = 2 m s^{-1}	v	v	u	u	r	r		
O = 80%; V = 1 m s^{-1}	v	u	u	r	r	r	d	r
O = 80%; V = 2 m s^{-1}	v	v	u	u	r	r	b	
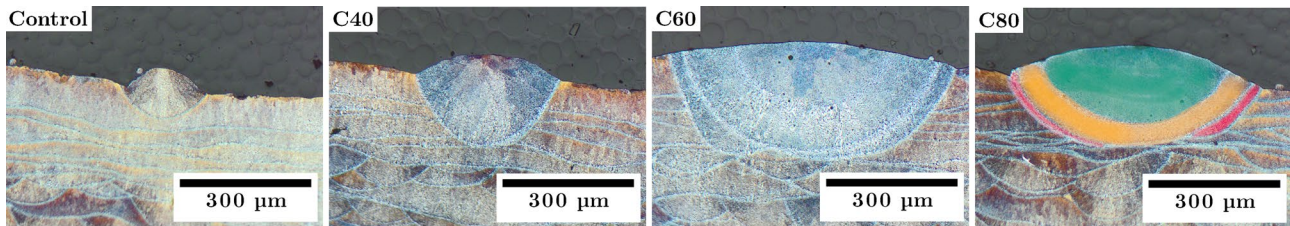
Fig. 7 100x microscope images of selected melt pools; C80's layers are highlighted
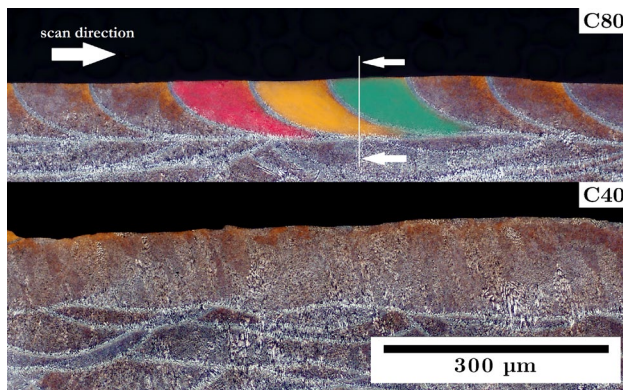
Fig. 8 Cross section parallel to scan direction of C80 and C40; scan direction and an estimated view plane of Fig. 7 depicted

Fig. 9 Porosity of C40, C60, and C80 parameter series

400 µm OD, and 1000 mm s^{-1} scan speed] for its relatively wide MP that spans 595 µm in width, C80 [80% overlap, 500 µm OD, and 2000 mm s^{-1} scan speed] for its high overlap percentage, and C40 [40% overlap, 300 µm OD, and 2000 mm s^{-1} scan speed] for its similarity to a control MP due to its relatively small U-shaped MP. For reference, all three are shown below in Fig. 7 as well as a control.

An additional MP shape discovered is the multi-layered MPs seen in Figs. 7 and 8. Each crescent is highlighted in a different color. The same MP is cross-sectioned in Fig. 8 in the scan direction with the same color coding. Both C60 and C80 exhibited this quality.

3.2 Porosity

The sample densities using the Archimedes density method are shown in Fig. 9. A broad range of porosities under 0.5% can be seen in all three parameter sets. The four control cubes had an average porosity of 0.272% also seen in Fig. 9 as a horizontal line. The respective MP width measured with the single MPs is also shown. Large deviations from the average density of the control cube are only present towards the largest hatching distances and the smallest hatching distance in the C60 data set. A general increase in porosity is seen as the distance between scan lines is increased. This increase was accelerated when cubes were printed with a hatching distance larger than their respective MP widths. Towards the lower hatching distances of C60 and C80 there is also an increase in porosity suggesting a range of hatching

distances that are more optimal. Both have their respective porosity minima between 470 and 500 µm.

To gain a better understanding of the distribution and shape of the aforementioned porosity in oscillating scan patterns as opposed to traditional scan lines, µCT scans were analyzed. Figure 10 shows a top view in the build direction of all reconstructed pores. The volume of the pores is color coded. The control cube possesses the highest detected porosity with the ten largest pores all in the center of the cube away from the contour interface with an average sphericity of 0.374 and a volume of 0.0107 mm³. The control cube manufactured by traditional parameters showed signs of balling due to the plate-shaped pores in Fig. 11 [33]. All three cubes have a higher concentration of pores along the interface between the contour and the hatching scan lines, but this is typical for all scan patterns using a contour-hatch scan strategy and is not a distinguishing factor for oscillating
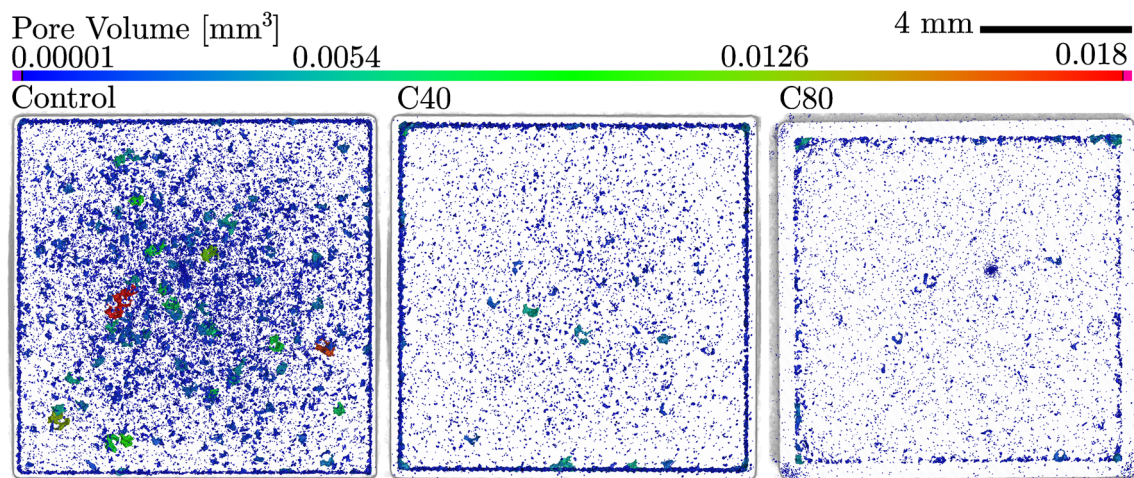

Fig. 10 µCT scan in build direction with highlighted pores and translucent cube sample

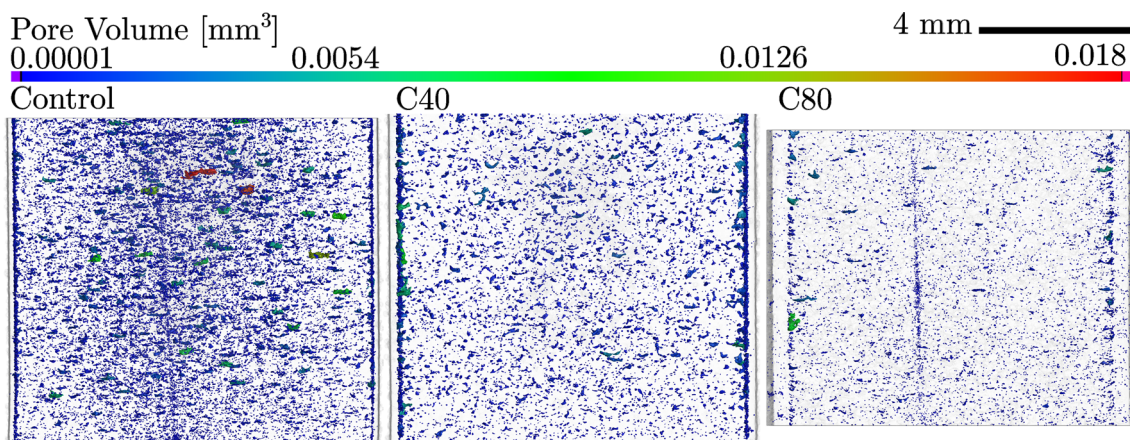**Fig. 11** µCT scan perpendicular to build direction with highlighted pores and translucent cube sample

Table 5 Porosity comparison between Archimedes and µCT methods

| Method	Control	C40	C80
Archimedes	0.187%	0.225%	0.431%
µCT	0.17%	0.10%	0.03%

scan lines. C80 using a hatching distance of 450 µm, possessing the largest MP width of the three, sees eight of its ten largest pores accumulated in the corners of the cube and have an average sphericity of 0.468 and a volume of 0.00387 mm^3. C40 with a hatching distance of 240 µm has a pore distribution that strays further from the corners and could be compared to a combination of the control cube and the C80 parameter set. The 10 largest pores have an average sphericity of 0.509 and a volume of 0.00553 mm^3. C40 and C80 drastically reduced the size of the largest pores found in the samples. The reduced contrast of µCT scans in the rotating axis is a common artifact that results in falsely identified pores most prominently displayed by the control

and C80 cubes in Fig. 11. A comparison between the density values gathered by the Archimedes and µCT methods is seen in Tabel 5.

3.3 Microstructure

Figure 12 is a comparison between the microstructure of a control cube and C60 with a hatching distance of 650 µm, which has a rectangular MP shape. The individual MPs are not in lateral contact on the last layer of C60, revealing the substrate of the previous layer. This spacing is seen between the two green highlighted MPs. There is an average of 97 µm between MPs, or in other words, 13.3% of the top layer consists of the material from the previous layer. This set of parameters still had a porosity level of 0.524% and did not show signs of a lack of fusion porosity.

SEM images were captured to observe the differences in eutectic cell structure between C40, C80, and the control parameters while also comparing with the literature. Seen in Fig. 13, is a comparison between the

(a)

(b)
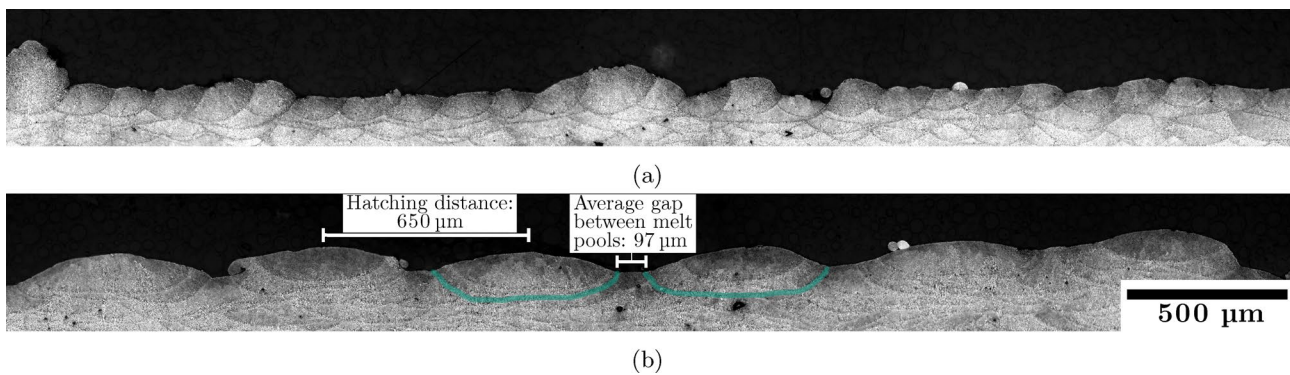
Fig. 12 Top layer cross section of **a** control cube and **b** C60 with a hatching distance of 650 µm
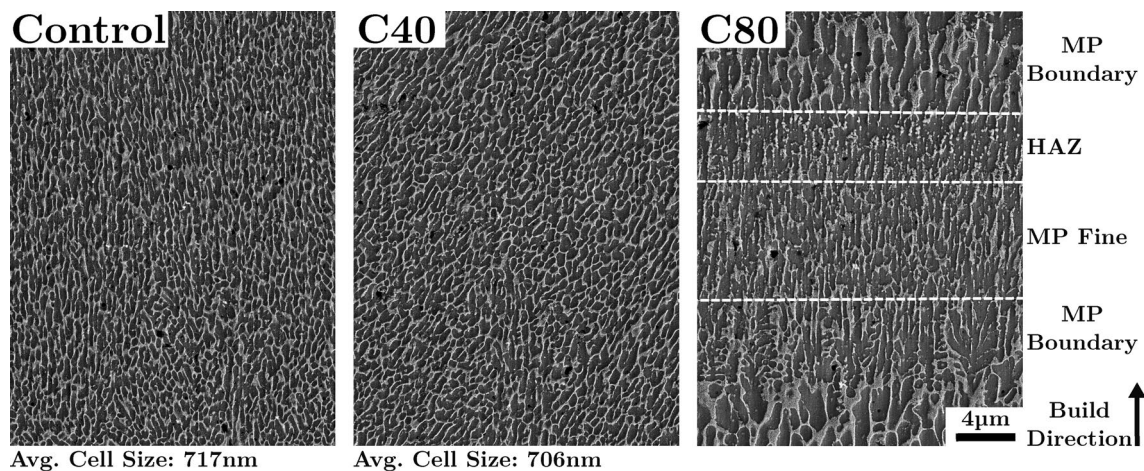
Fig. 13 SEM images of an etched cross section of Control, C40, and C80 parameters in the center of their respective melt pools (MP)

three aforementioned cell structures in the center of their respective MPs while also labeling the three different layers found in the L-PBF MP microstructure [6, 24]. The control and C40 images show similar fine cell structures. This similarity despite C40 being printed with double the scan speed further explains the similarities seen between their mechanical properties. Due to the depth of each C80 MP without changing the 30 μm layer thickness, the cube cross section consists of mostly MP boundary and heat-affected-zone (HAZ) creating a novel microstructure. This is why cell size was not a reasonable measurement. Due to the rectangular MP shape having a relatively flat bottom-out, the cell structure is oriented exclusively in build direction.

3.4 Surface Roughness

The use of oscillating scan lines had a significant effect on the surface quality of the samples manufactured in this study. The surface of the reference parameter set shown in Fig. 14 is characterized by a high-frequency periodic morphology produced by the hatching of the individual laser paths. In the scan direction, the roughness is nonperiodic. This is caused by instability of the MP, uneven distribution of powder across the surface, and the spatter exiting the keyhole and landing on the already manufactured surface. C80, due to its large and stable MP, shows significant differences from the control cube. The periodic nature of an L-PBF manufactured part is still evident, but at a much lower frequency because of the much larger scan lines. A
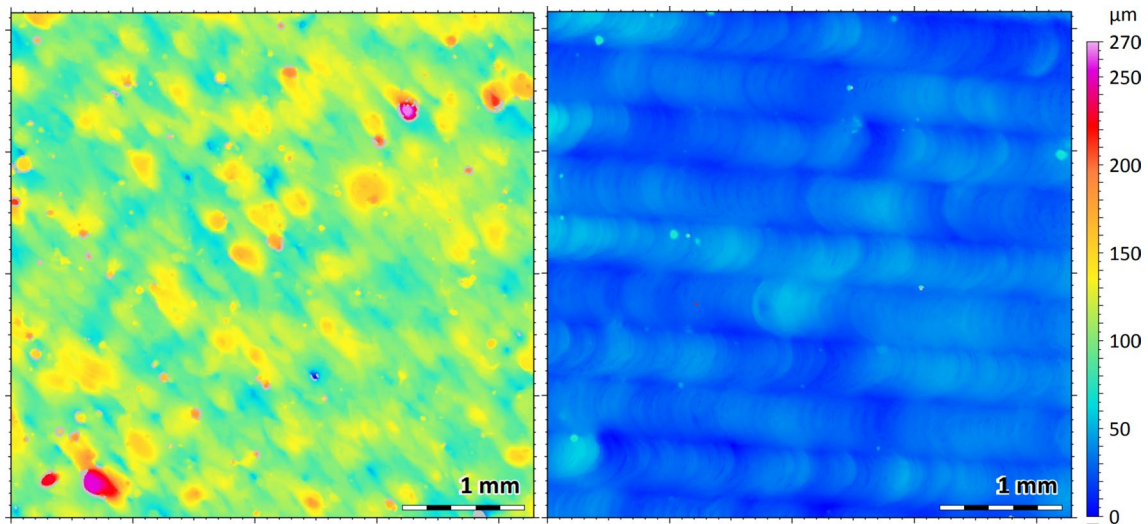
Fig. 14 Top layer topography of a control cube (left) and C80 with a hatching distance of 450 μm (right)
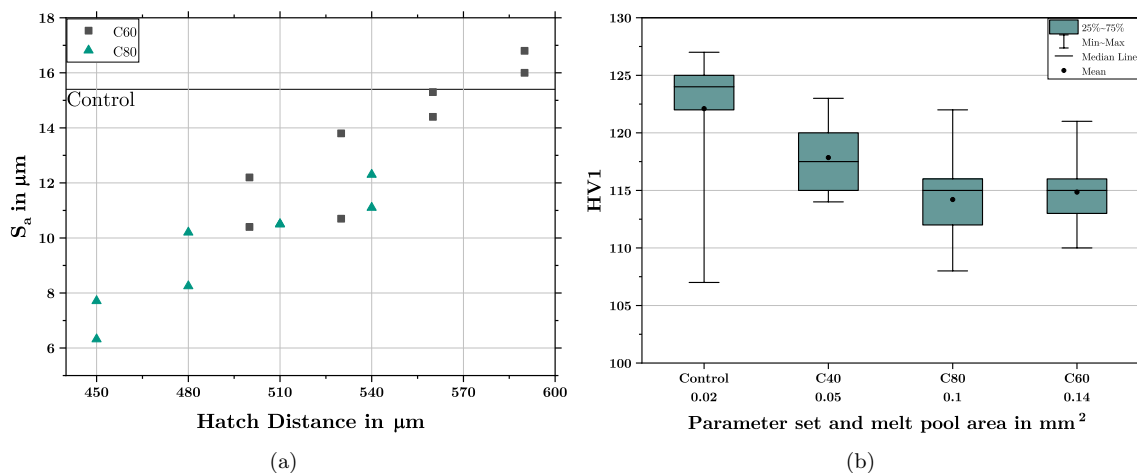
Fig. 15 **a** S_a of the top layer vs. hatching distance for C60 and C80 cubes, **b** HV1 hardness vs. melt pool cross-section area

new periodic surface feature is visible in the direction of the scan lines due to the oscillating laser which is similar to a weld often referred to as chevrons. Additionally, much fewer abnormalities due to spatter are present on the C80 cube bringing its S_z value down to 78.4 μm as opposed to the control value of 266 μm. A positive correlation between hatching distance and surface roughness reveals itself for C60 and C80 which stays consistent for both trials (Fig. 15a). For comparison, the control cube had an S_a value of 15.4 μm displayed as a horizontal line in Fig. 15a.

3.5 Microhardness

All twelve cubes that were polished and etched were also tested ten times for microhardness using the HV1-10s standard. Figure 15b plots this hardness value against the area of the MP for each parameter set which was determined metallographically. The precedent set by the two control cubes measured is an average of 122.17 HV1 which was never reached using the new parameter sets. Two values that do correlate with a statistical significance at the 0.05 level using the Kendall Method are the cross-sectional area of the MP in

mm^2, using the area of the MP from the single MP samples, and the HV1 hardness seen in Fig. 15b [34].

3.6 Tensile Strength

The data gathered from the tensile stress tests of ten control specimens, ten C80 specimens, and ten C40 specimens is seen in Figs. 16 and 17. In Fig. 16 a representative stress–strain curve of the three parameters tested can be seen. The control specimen exhibits the typical brittle stress–strain curve of a L-PBF manufactured aluminum specimen. C40 and C80 sacrifice some maximum yield stress while increasing their elongation at fracture. The same can be seen in Fig. 17 where all ultimate tensile strength, yield strength, and elongation at the point of fracture values are shown for all tensile tests.

4 Discussion

4.1 Differentiating a "Unified MP" from a "Stacked MP"

Significant evidence has been gathered that oscillating MPs are not to be judged based on their top surface quality alone. C80 in Fig. 7 reveals that when the laser loops back on its oscillating path, the previous loop has already solidified. In other words, C80 is made up of many spiraled small traditional scan lines rather than building a large MP. The pink MP in Fig. 8 is not seen crossing the view plane, but can be seen in Fig. 7. This can be attributed to the fact that it is not known exactly where the MP viewed in Fig. 8 is cross-sectioned.

The consequence of this finding is that if a thorough study of oscillating scan lines is attempted the cross section running parallel to the scan direction is needed for a full understanding of the MP at hand. In the following chapters, this study will coin the term *stacked MP* for clarification.
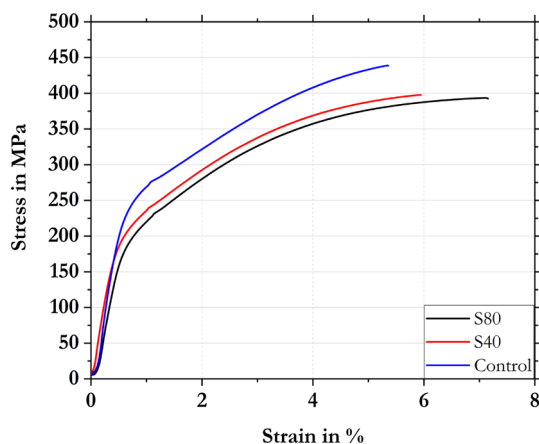

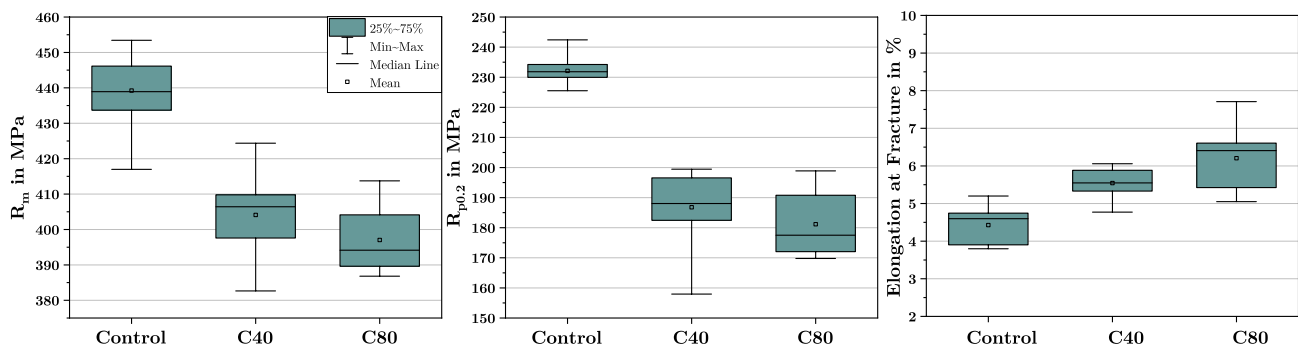**Fig. 16** An example stress–strain diagram for C80, C40, and control

Fig. 17 R_m, $R_{p0.2}$, and the elongation at fracture distributions of C80, C40, and control

Assuming that a MP is unified does not mean that it necessarily has the properties expected from having a large MP. In theory, what this new subset of MP forms has created are long scan pattern islands filled with singular oscillation paths. The confounding part of this finding is that these new stacked MPs still possess the qualities expected from a larger MP in terms of hardness and strength. The stacked MPs of C80 and C60 had lower hardness and strength values than C40. One way to explain this is that even though the previous loop of the oscillation has solidified in a stacked MP, does not mean that it is not still relatively hot compared to the rest of the sample and subsequently becomes reheated for a second and possibly a third time in rapid succession. This is compounded with the higher percentage of coarse boundary layer in the build direction seen in Fig. 13. Therefore, the properties of a large MP persist with the sample size seen in this study.

4.2 Porosity comparison

The large variance between values seen in Table 5 can be attributed to several common sources of error with either measurement technique. Due to the resolution of the µCT scan, micropores are imperceptible, additionally, the rough surface of AM parts can lead to bubbles being trapped as the sample is submerged into the water in the Archimedes density measurement. Both sources of error lead to the µCT scan porosity analysis underestimating the porosity and the Archimedes method overestimating [35]. It is assumed that C80 with a hatching distance of 450 µm had numerous micropores or its rough side surface trapped a considerable amount of air when submerged, despite the measures taken to counteract this effect as described in Sect. 2.2.

4.3 The use of large MPs

Most of the findings of this study can be attributed to the size, in width and depth, of the MPs at hand. For reference, a traditional L-PBF MP and the control parameters of this study produce an average MP width of 209 µm with a depth of 118 µm. The smallest optimized set of parameters, C40, still measured 316 µm in width and 210 µm in depth. The sizable difference between some of the larger MPs analyzed and the control parameters is the root cause of the reparation qualities, increase in ductility, and pore distribution.

The larger suitable range of hatching distances to create a high-density final product compared to traditional linear scan lines should be valued positively. If the goal is to stay below 0.5% porosity, then with an overlap of 80%, OD of 500 µm, and a laser speed of 2000 mm s^{-1} the range of acceptable hatching distances spans 150 µm from 390 to 540 µm. This range could be even larger if more extreme hatching distances are tested in future research. This can

also be compared to the 60 µm range between 130 µm and 190 µm of hatching distances found to stay under 0.5% porous with traditional scan lines while printing a more complex shape than a cube [29]. With an overlap of 60%, OD of 400 µm, and laser speed of 1000 mm s^{-1}, a hatching distance of 620 µm was used while staying beneath the 0.5% porosity benchmark. This parameter set had an average MP width of 580 µm, so the ability to manufacture high-density parts with a hatching distance larger than the nominal MP width is an interesting finding. This could also help combat the inherently slower manufacturing speed to the remelting of previous laser paths. This can be further improved by selectively using oscillating scan lines only where they are needed for their reduced porosity, increased pore sphericity, and increased process robustness.

The theory behind the broad range of acceptable hatching distance while using oscillating scan lines is the repairability due to MP size. Any lack-of-fusion gap has multiple chances of becoming remelted while using the C60 parameter set because of its 267 µm average depth and a layer being 30 µm deep. Adding to this effect is the rectangular MP shape often seen in the optimal zone of oscillation parameters. At this maximum depth the C60 MP exhibits a relatively flat boundary to previous layers which increases the chance that a previous pore is remelted because instead of a single point reaching the maximum depth like a U-shaped MP, it is an entire line [36]. In other words, the C60 MP has a large cross-section area that can remelt pores, giving them a chance to be filled with molten material. Important to note is that this process is dependent on the layer rotation. Changing this study's 67° layer rotation will change the chance that a pore will be covered in the following layers. Regardless, the repairability of previous layers is an attribute that sets these oscillating laser scan patterns apart. Additionally, the pores that were present had a higher average sphericity in comparison to the control sample because the typically non-spherical, plate-shaped balling pores were avoided due to this higher remelting chance and the decreased likelihood of Plateau-Rayleigh instabilities. This is an especially promising attribute for notch effect-sensitive properties such as the fatigue limit.

The higher porosity in the corners of the cube samples can also be attributed to the larger width of the oscillating MPs. To understand this relationship, the ORLAS Creator's minimum laser on-state duration of 0.25 ms plays an important role. The slicer makes the cutoff at a distance of 500 µm which is the distance that a 2000 mm s^{-1} linear scan line travels in the minimum of 0.25 ms without taking into account the added time needed for the oscillating scan lines. This means that scan lines are deleted prematurely from the Gcode used to control the printer when oscillating scan lines are used. Under the assumption that an L-PBF MP, when viewed from above, has the shape of an oblong,
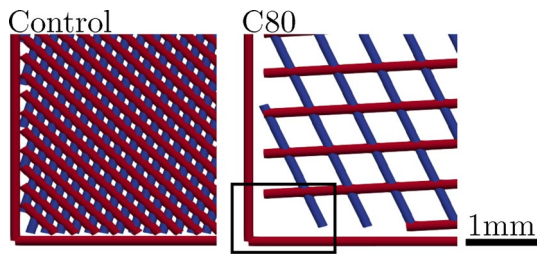
Fig. 18 Rendering of layers 399 (blue) and 400 (red) of the control cube and C80

two semicircles connected with two tangential lines at their endpoints, an estimate of the impact of the slicer's path deletion can be made. When a traditional MP, V=1000 mm s^{-1}, and width of 209 µm, 0.25 mm in length is deleted, it leaves an estimated area of 86557 µm^2 unmelted, while a C80 MP would leave 507139 µm^2 unmelted. The areas where most scan lines are deleted are the areas of the part with finer details, for example, depending on the layer rotation, the corners of the cubes. This is exactly where the most porosity was seen in the µCT scans done of C80 in Fig. 10. A rendering of two layers of scan lines stacked on top of each other is seen in Fig. 18. In the black box should be another blue scan line, but it was deleted leading to an increased chance of porosity forming in this corner. With a custom Gcode program this limitation could be avoided, which adds to the untapped potential of oscillating scan lines and opens the door for future research.

Therefore, the theoretical density improvement that oscillating scan lines possess due to the increase in MP stirring has yet to be proven because of the accumulation of pores in the corners skewing the porosity results. Conversely, strong signs supporting the theoretical resilience of the oscillating paths against balling has been seen in this study when comparing the pore shape of C80 to the control cube in Fig. 11. In other words, the global porosity increased slightly, but the average size of the pores was reduced as a result of the reduction of balling related pores.

4.4 Tuning Mechanical Properties by Changing Oscillation Parameters

The size of the MP is also closely related to the mechanical properties of the manufactured part. Just like an air-cooled cast aluminum part will usually have a lower hardness but more ductility than a quenched part, a large MP has a lower hardness but more ductility than a smaller, traditional MP [37]. This correlation translates into a change in cell size due to the solidification rates. In a small MP, there is more thermally conductive solid metal in close proximity to pull the heat away, so the cooling rate increases. This is the explanation for the correlation seen in Fig. 15b. The lack of a

statistically significant difference between the hardness of C60 and C80 points to the fact that the relationship between the MP area and the hardness is not linear. An accurate observation of this relationship would require a larger range of MP cross-sectional areas and a larger sample size for each. Furthermore, the correlation could differ for stacked MPs, C80 and C60, and unified MPs, C40, due to different solidification behaviors.

The rectangular MP shape also has an effect on the solidification direction and therefore microstructure of the resulting sample. The cell structure oriented strongly in the build direction of C80 in Fig. 13 points towards the thermal gradient during solidification and grain orientation also being oriented in build direction which further sets C80 apart from traditional parameter sets. Furthermore, the large amount of cross-sectional area attributed to the coarse MP boundary is a likely factor for the increased ductility of the C80 parameter set. The active selection of a parameter set that combines a stacked MP and a deep MP in comparison to the layer height is a technique that can be recommended based on the results of this study.

The comparison of the mechanical effects seen in this study to other research in the field is difficult due to the unique capabilities of laser oscillation. The striped island scan patterns are typically one cm in width, so the effects are not comparable with the oscillating scan lines. The negligible effect on the mechanical properties using a striped scan island pattern proves this [38, 39]. The process parameter that comes closest to the effects seen here is the implementation of other laser beam profiles such as the donut shape [40]. Here, the same increase in MP width can be observed, but on a different scale as in this study with a width of up to 350 µm but keeping the U-shaped MP. The optimization for donut-shaped beam profiles performed by Wischeropp et al. is similar to what this study does for oscillating scan lines, but it does not test hardness, tensile strength, yield strength, and ductility, which would help to see if the oscillating scan lines are having the same effect on the microstructure. In conclusion, the striped scan patterns seen today are too large to affect the mechanical properties in the same way as observed in this study, and changing the beam profile seems to have a similar effect on the MP, but has not been researched extensively enough yet.

The recipe for creating a large MP has been formed through the result of this study as well. Increasing the diameter of the oscillation is the first logical step. To stabilize this expansion an increase of the overlap or reduction in laser scan speed is needed to close the gaps between loops. This can be seen in Table 4 where the only overlaps that created a unified MP at a diameter of 600 µm were 60% and 80%. Increasing the diameter and overlap also happens to be the theorized recipe to create a stacked MP because the time between loops increases with the diameter, and the increase

in overlap makes the MP appear to be unified when viewed from above. The increased time between loops allows for the solidification of that path before the laser returns for the next loop. In this study, C60 and C80 exhibited a stacked MP but still exhibited the mechanical properties of a large MP, but this study puts forth the hypothesis that these stacked MPs eventually, with increased OD, will tend towards showing the properties of a traditional MP. The previous loop of the stacked MP will have had a comparable amount of time to cool down to neighboring traditional scan lines, similar to a striped scan island pattern if the diameter is increased further and further. Based on the data gathered in this study, it is not clear when this transition is made, but the statistically insignificant difference between the hardness of C80 and C60, seen in Fig. 15b despite the increase in MP area might mark the turning point. Further research is needed to find the postulated minimum in hardness and corresponding ultimate tensile strength, ductility, and yield strength before the values start closing in on the values seen in traditional scan patterns.

5 Conclusion

The mechanical effects and general behavior of oscillating laser paths with the use of AlSi10Mg have been observed in this study. Through the use of 72 single MPs, 48 cubes, and 30 tensile strength specimens a large set of parameters were narrowed down to two sets that exhibit differentiating mechanical properties. This study not only tested the extreme ranges of oscillation parameters but also provided insight into AlSi10Mg's behavior in response to oscillating scan lines.

- Unified MPs were found up to 919 µm in width and as small as 274 µm. All MPs were larger than the traditional scan track which had a width of 209 µm. Twelve out of the 14 MPs in this optimal zone had a rectangular MP shape.
- With 60% overlap, an OD of 400 µm, and an absolute laser scan speed of $1000\,\mathrm{mm\,s^{-1}}$, a cube with under 0.5% porosity was created with a hatching distance between 440 and 620 µm. This large range of values sets oscillating scan lines apart from linear scan paths due to ease of optimization and process robustness. Hatching distances larger than the principle MP width were found to still yield dense cuboid samples.
- Up to a 70% reduction in final layer surface roughness in comparison to the control strategy can be achieved with certain combinations of parameters like C80.
- Oscillation parameters caused a strong decrease in balling pores and instead had an accumulation of pores in the corners of the cubes because of the slicing method used.

- With an overlap of 80%, 500 µm OD, and $2000\,\mathrm{mm\,s^{-1}}$ laser scan speed an average 40% increase in the elongation at fracture was achieved while reducing the ultimate tensile strength by 10% on average in comparison to the specimens using the control parameters.

Lastly, this study opens the door to several other research topics regarding oscillating laser scan lines. For example, pinpointing the transition from unified MPs to stacked MPs, manufacturing with a hatching distance above the MP width, manufacturing more complex geometries, fatigue testing, and the targeted use of oscillating scan lines in high load points of interest can now be researched with the applied optimized scan lines outlined in this paper.

Declarations

References

1. DebRoy T, Wei HL, Zuback JS, Mukherjee T, Elmer JW, Milewski JO, Beese AM, Wilson-Heid A, De A, Zhang W (2018) Additive manufacturing of metallic components—process, structure and properties. Progress Mater Sci 92:112–224

2. Buchbinder D, Schleifenbaum H, Heidrich S, Meiners W, Bültmann J (2011) High power selective laser melting (HP SLM) of aluminum parts. Phys Proc 12:271–278

3. Yadroitsev I, Smurov I (2010) Selective laser melting technology: from the single laser melted track stability to 3D parts of complex shape. Phys Proc 5:551–560

4. Bayat M, Thanki A, Mohanty S, Witvrouw A, Yang S, Thorborg J, Tiedje NS, Hattel JH (2019) Keyhole-induced porosities in Laser-based Powder Bed Fusion (L-PBF) of Ti6Al4V: high-fidelity modelling and experimental validation. Addit Manuf 30:100835

5. Xing W, Lyu T, Chu X, Rong Y, Lee C-G, Sun Q, Zou Y (2021) Recognition and classification of single melt tracks using

deep neural network: a fast and effective method to determine process windows in selective laser melting. J Manuf Process 68:1746–1757

6. Hyer H, Le Zhou S, Park G, Gottsfritz G, Benson B, Tolentino B, McWilliams K. Cho, Sohn Y (2020) Understanding the laser powder bed fusion of AlSi10Mg alloy. Metallogr Microstruct Anal 9(4):484–502

7. Schniedenharn M (2020) Einfluss von Fokusshift und Prozessnebenprodukten auf den Laser Powder Bed Fusion Prozess. Dissertation, Apprimus Verlag, Rheinisch-Westfälische Technische Hochschule Aachen

8. Bonhoff T, Schniedenharn M, Stollenwerk J, Loosen P (2017) Experimental and theoretical analysis of thermo-optical effects in protective window for selective laser melting. In: Proceedings of the International Conference on Lasers in Manufacturing LiM, Munich, Germany, pp. 26–29

9. Hu J-F, Yang J-G, Fang H-Y, Li G-M, Zhang Y (2006) Numerical simulation on temperature and stress fields of welding with weaving. Sci Technol Weld Join 11(3):358–365

10. Tasalloti H, Kah P, Martikainen J (2014) Effects of welding wire and torch weaving on GMAW of S355MC and AISI 304L dissimilar welds. Int J Adv Manuf Technol 71(1–4):197–205

11. Guzman-Flores I, Vargas-Arista B, Gasca-Dominguez JJ, Cruz-Gonzalez CE, González-Albarrán MA, del Prado-Villasana J (2017) Effect of torch weaving on the microstructure, tensile and impact resistances, and fracture of the HAZ and weld bead by robotic GMAW process on ASTM A36 steel. Soldagem & Inspeção 22(1):72–86

12. Wang L, Gao M, Zhang C, Zeng X (2016) Effect of beam oscillating pattern on weld characterization of laser welding of AA6061-T6 aluminum alloy. Mater Des 108:707–717

13. Börner S, Dittrich D, Mohlau P, Leyens C, García-Moreno F, Kamm PH, Neu TR, Schlepütz CM (2021) In situ observation with x-ray for tentative exploration of laser beam welding processes for aluminum-based alloys. J Laser Appl 33(1):012026

14. Choi K-D, Ahn Y-N, Kim C (2009) Weld strength improvement for Al alloy by using laser weaving method. In: International Congress on Applications of Lasers & Electro-Optics. Laser Institute of America, pp. 182–185

15. Yang H, Jing G, Gao P, Wang Z, Li X (2020) Effects of circular beam oscillation technique on formability and solidification behaviour of selective laser melted Inconel 718: From single tracks to cuboid samples. J Mater Sci Technol 51:137–150

16. Louvis E, Fox P, Sutcliffe CJ (2011) Selective laser melting of aluminium components. J Mater Process Technol 211(2):275–284

17. Matthias S, Lucas M, Sivam S (2019) Using wobble based laser scanning techniques in additive manufacturing applications. In: Lasers in Manufacturing Conference

18. Gusarov AV, Yadroitsev I, Bertrand P, Smurov I (2007) Heat transfer modelling and stability analysis of selective laser melting. Appl Surf Sci 254(4):975–979

19. Islam N, Schanz J, Kolb D, Riegel H (2021) Improvement of surface quality and process area rate in selective laser melting by beam oscillation scan technique. J Mater Eng Perform 30(7):5108–5117

20. Huang T-Y, Cheng C-W, Lee A-C, Chang T-W, Tsai M-C (2023) Influence of wobble-based scanning strategy on surface morphology of laser powder bed-fabricated permalloy. Materials (Basel, Switzerland) 16(5):2062

21. Tang M, Pistorius PC, Beuth JL (2017) Prediction of lack-of-fusion porosity for powder bed fusion. Addit Manuf 14:39–48

22. Zyguła K, Nosek B, Pasiowiec H, Szysiak N (2018) Mechanical properties and microstructure of AlSi10Mg alloy obtained by casting and SLM technique. World Sci News 104:456–466

23. Cao Y, Lin X, Wang QZ, Shi SQ, Ma L, Kang N, Huang WD (2021) Microstructure evolution and mechanical properties at high temperature of selective laser melted AlSi10Mg. J Mater Sci Technol 62:162–172

24. Kempf A, Hilgenberg K (2020) Influence of sub-cell structure on the mechanical properties of AlSi10Mg manufactured by laser powder bed fusion. Mater Sci Eng A 776:138976

25. Santos Macías JG, Elangeswaran C, Zhao L, Buffière J-Y, van Hooreweder B, Simar A (2021) Fatigue crack nucleation and growth in laser powder bed fusion AlSi10Mg under as built and post-treated conditions. Mater Des 210:110084

26. Xiong F, Gan Z, Chen J, Lian Y (2022) Evaluate the effect of melt pool convection on grain structure of IN625 in laser melting process using experimentally validated process-structure modeling. J Mater Process Technol 303:117538

27. Luo Q, Yin L, Simpson TW, Beese AM (2022) Effect of processing parameters on pore structures, grain features, and mechanical properties in Ti-6Al-4V by laser powder bed fusion. Addit Manuf 56:102915

28. Schindelin J, Arganda-Carreras I, Frise E, Kaynig V, Longair M, Pietzsch T, Preibisch S, Rueden C, Saalfeld S, Schmid B et al (2012) Fiji: an open-source platform for biological-image analysis. Nat Methods 9(7):676–682

29. Englert L, Czink S, Dietrich S, Schulze V (2022) How defects depend on geometry and scanning strategy in additively manufactured AlSi10Mg. J Mater Process Technol 299:117331

30. International Organization for Standardization (2019) DIN EN ISO 6892–1:2019, Metallic materials - Tensile testing - Part 1: Method of test at room temperature. Beuth Verlag GmbH, Berlin, Deutschland

31. International Organization for Standardization (2012) DIN EN ISO 25178–2:2012–09, Geometrical Product Specifications (GPS) Surface Texture: Areal Part 2: Terms, Definitions and Surface Texture Parameters. Beuth Verlag GmbH, Berlin, Deutschland

32. American Society for Testing and Materials (2013) Standard Test Methods for Determining Average Grain Size, E 112–96. ASTM International, West Conshohocken, PA, USA

33. Aboulkhair NT, Everitt NM, Ashcroft I, Tuck C (2014) Reducing porosity in AlSi10Mg parts processed by selective laser melting. Addit Manuf 1–4:77–86

34. Kendall MG (1938) A new measure of rank correlation. Biometrika 30(1–2):81–93

35. Spierings A B, Schneider M, Eggenberger R (2011) Comparison of density measurement techniques for additive manufactured metallic parts, Rapid Prototyping J 17(5):380–386

36. Tang M (2017) Inclusions, porosity, and fatigue of AlSi10Mg parts produced by selective laser melting. Carnegie Mellon University, Doctor of Philosophy

37. Liu M, Zhang Z, Breton F, Chen X-G (2019) Investigation of the quench sensitivity of an AlSi10Mg alloy in permanent mold and high-pressure vacuum die castings. Materials (Basel, Switzerland) 12(11):1876

38. Yadav P, Rigo O, Arvieu C, Lacoste E (2022) Microstructural and mechanical aspects of AlSi7Mg0.6 alloy related to scanning strategies in L-PBF. Adv Manuf Technol 120(9):6205–6223

39. Mugwagwa L, Dimitrov D, Matope S, Yadroitsev I (2019) Evaluation of the impact of scanning strategies on residual stresses in selective laser melting. Int J Adv Manuf Technol 102(5–8):2441–2450

40. Wischeropp TM, Tarhini H, Emmelmann C (2020) Influence of laser beam profile on the selective laser melting process of AlSi10Mg. J Laser Appl 32(2):022059